Reconciling different approaches to quantifying land surface temperature impacts of afforestation using satellite observations

Huanhuan Wang[1], Chao Yue[2,3*], Sebastiaan Luyssaert[4]

[1]College of Natural Resources and Environment, Northwest A&F University, Yangling, Shaanxi 712100, P. R. China

[2] State Key Laboratory of Soil Erosion and Dryland Farming on the Loess Plateau, Northwest A&F University, Yangling, Shaanxi 712100, P. R. China

[3] College of Forestry, Northwest A&F University, Yangling, Shaanxi 712100, P. R. China

[4] Department of Ecological Sciences, Faculty of Sciences, Vrije Universiteit Amsterdam, Amsterdam 1081 HV, The Netherlands

Correspondence: Chao Yue, State Key Laboratory of Soil Erosion and Dryland Farming on the Loess Plateau, Northwest A&F University, Yangling, Shaanxi 712100, P. R. China

E-mail: chaoyue@ms.iswc.ac.cn

Abstract

Satellite observations have been widely used to examine afforestation effects on local surface temperature at large spatial scales. Different approaches, which potentially lead to differing definitions of the afforestation effect, have been used in previous studies. Despite their large differences, the results of these studies have been used in climate model validation and cited in climate synthesis reports. Such differences have been simply treated as observational uncertainty, which can be an order of magnitude bigger than the signal itself. Although the fraction of the satellite pixel actually afforested has been noted to influence the magnitude of afforestation effect, it remains unknown whether it is a key factor which can reconcile the different approaches. Here, we provide a synthesis of three influential approaches (one

1

estimates the actual effect and the other two the potential effect) and use large-scale afforestation over China as a test case to examine whether the different approaches can be reconciled. We found that the actual effect (ΔT_a) often relates to incomplete afforestation over a medium resolution satellite pixel (1km). ΔT_a increased with the afforestation fraction, which explained 89% of its variation. One potential effect approach quantifies the impact of quasi-full afforestation (ΔT_{p1}), whereas the other quantifies the potential impact of full afforestation (ΔT_{p2}) by assuming a shift from 100% openland to 100% forest coverage. An initial paired-samples *t*-test shows that $\Delta T_a < \Delta T_{p1} < \Delta T_{p2}$ for the cooling effect of afforestation ranging from 0.07K to 1.16K. But when all three methods are normalized for full afforestation, the observed range in surface cooling becomes much smaller (0.79K to 1.16K). Potential cooling effects have a value in academic studies where they can be used to establish an envelope of effects, but their realization at large scales is challenging given its nature of scale dependency. The reconciliation of the different approaches demonstrated in this study highlights the fact that the afforestation fraction should be accounted for in order to bridge different estimates of surface cooling effects in policy evaluation.

Keywords: surface temperature change, afforestation, actual effect, potential effect, reconciliation, surface energy balance, China

1 Introduction

Afforestation has been and is still proposed as an effective strategy to mitigate climate change because forest ecosystems are able to sequester large amounts of carbon in their biomass and soil, slowing the increase of atmospheric CO_2 concentration (Fang et al., 2014; Pan et al., 2011). Additionally, forests regulate the exchange of energy and water between the land surface and

the lower atmosphere through various biophysical effects, including radiative processes such as surface reflectance, and non-radiative processes such as evapotranspiration and sensible heat flux (Bonan, 2008; Juang et al., 2007). As the net result of the surface energy balance, land surface temperature (LST) is widely used to measure the local climatic impact of afforestation (Li et al., 2015; Winckler et al., 2019a).

Climate model simulations and site-level observations have been utilized to explore the impact of forest dynamics on land surface temperature (Lee et al., 2011; Pitman et al., 2009; Swann et al., 2012). However, afforestation impacts on local LST derived from models tend to be highly uncertain as they are limited by the coarse spatial resolution of models and uncertainties in model parameters and processes (Oleson et al., 2013; Pitman et al., 2011), while insights from site-level assessments cannot be extrapolated to large spatial domains (Lee et al., 2011). Alternatively, remote sensing-based LST products enable the assessment of local LST changes due to forest dynamics on large spatial scales (Li et al., 2015; Shen et al., 2020).

A number of studies investigated the surface temperature impact of afforestation based on satellite observations and they have been cited in high-level climate science synthesis reports (e.g., *IPCC Special Report on Climate and Land* authored by Jia et al., 2019), even though there are large differences in afforestation impacts on LST between different methods. For example, Alkama and Cescatti (2016), found a cooling effect of about 0.02K from afforestation in temperate regions, while Li et al. (2015) reported a 0.27±0.03K 'potential' cooling from afforestation in the northern temperate zone (20–50° N) based on the 'space-for-time' method. In contrast, Duveiller et al. (2018) found a much stronger 'potential' cooling effect of 2.75K for afforestation in the northern temperate region. While such differences were acknowledged in a recent modelling study (Winckler et al., 2019b), they were simply treated as observational

76 uncertainty for climate model evaluation, with the uncertainty range being as big as, or even an

77 order of magnitude larger than, the afforestation effect. It remains unclear whether the

78 differences arising from these different methods can be reconciled.

79

80 Until now, studies using satellite data to investigate afforestation impact on surface temperature

81 have mainly focused on three methods. The first method, termed the 'space-and-time' approach

82 (Fig. 1, red box), aims to examine the actual, realized effect of afforestation ('actual effect') by

83 isolating the forest cover change effect from the gross temperature change over time in places

84 where forest cover change actually occurred (Alkama and Cescatti, 2016; Li et al., 2016a). The

85 second method, termed the 'space-for-time' approach (Fig. 1, orange box), compares the

86 surface temperature of forest with adjacent 'openland' (i.e., cropland or grassland) under similar

87 environmental conditions (e.g., background climate and topography) and estimates the

88 'potential effect' of afforestation if afforestation were to occur (Ge et al., 2019; Li et al., 2015;

89 Peng et al., 2014). Note that such effects are often quantified using medium-resolution land-

90 cover datasets (typical resolution = 1km), which do not necessarily represent 100% ground

91 coverage, and we therefore term such a potential effect a 'mixed potential effect'.

92

93 The third method, recently used by Duveiller et al. (2018), uses the 'singular value

94 decomposition' technique (Fig. 1 green box), which is claimed to extract the hypothetical LST

95 for different land-cover types by assuming a 100% coverage of the target cover type. The

96 afforestation effect on LST is then quantified as the difference between the LST of a pixel with

97 a hypothetical 100% forest coverage and the LST of an adjacent pixel with 100% openland

98 coverage. As with the second method, such an approach quantifies the 'potential effect' of

99 afforestation, but in this case, it quantifies the 'full potential effect' by assuming transitions

100 between land-cover types with 100% complete ground coverage.

101 Previous studies have revealed the fraction of forest change as an important factor determining

102 the magnitude of the afforestation effect. Alkama and Cescatti (2016) indicated that the actual

103 temperature effect is fraction-dependent, and Li et al. (2016a) pointed out that use of a higher

104 threshold to define forest change resulted in a stronger potential effect. Nonetheless, whether

105 the fraction of forest change can explain the differences in the afforestation effect produced by

106 different methods, e.g., whether the 'potential' effect can be 'actualized', has not been

107 demonstrated. Testing the role of afforestation fraction in reconciling the afforestation effects

108 produced by different methods can help clarify potential confusion and contribute to appropriate

109 policy evaluation.

110

111 This study develops detailed conceptual and methodological descriptions for each of the three

112 approaches and uses large-scale afforestation over China as a case study to compare the three

113 approaches. We tested the following hypotheses: (1) The actual effect on LST increases with

114 the area that has actually been afforested, defined as afforestation intensity (or F_{aff}). (2) The

115 actual effect is smaller than the potential effects. (3) When extending F_{aff} to a hypothetical value

116 of 100%, the actual effect approaches the potential effect. If proven, this third hypothesis

117 implies that the LST impacts from different approaches could be reconciled given the same

118 boundary condition of full afforestation. In that case, we then have a fourth hypothesis (4)

119 stating that changes in underlying biophysical processes including radiation, sensible and latent

120 heat fluxes that drive LST changes should also be reconciled among different methods. To keep

121 the focus on reconciling methodological differences, only changes in the daytime surface

122 temperature were considered in this study. Nevertheless, similar conclusions regarding the

123 different approaches are expected for nighttime surface temperature.

124
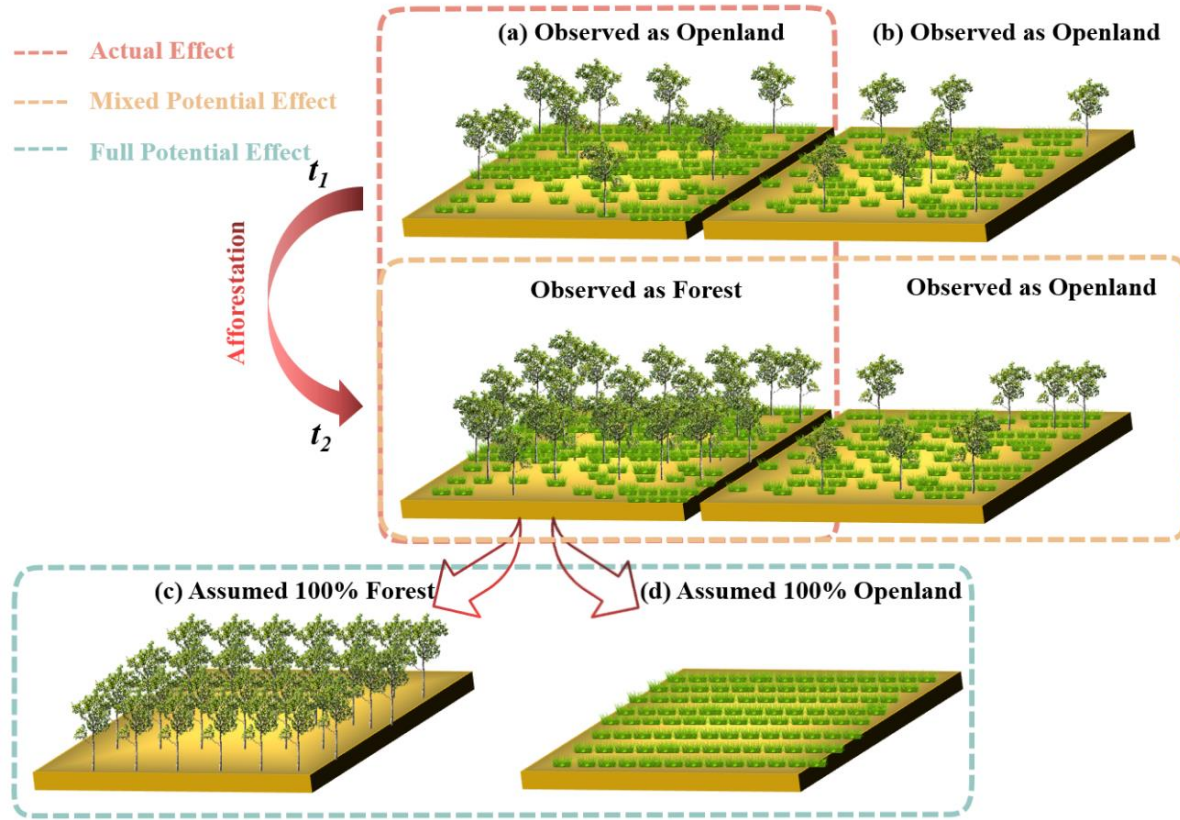
Figure 1. Illustration of the three approaches to quantifying the local surface temperature effect of afforestation. (a) and (b) represent two nearby pixels, both classified as openland at time t_1 by medium-resolution satellites (1km spatial resolution), with one of them classified as forest at time t_2 (i.e., having experienced afforestation) and the other unchanged. Note, neither of these pixels will have 100% complete coverage of either openland (i.e., grassland or cropland) or forest, but they will have been classified as either openland or forest by medium-resolution satellite products. (c) and (d) represent pixels with 100% forest or 100% openland coverage whose temperature can be derived from pixels of mixed land cover types by using the singular value decomposition (SVD) technique (Duveiller et al., 2018). The red dotted box describes the quantification of the 'actual effect' of afforestation (ΔT_a) occurring from t_1 to t_2 by the 'space-and-time' method. The orange box represents the 'mixed potential effect' determined by hypothesizing potential shifts between openland and forest based on the 'space-for-time' approach (ΔT_{p1}). The green box represents the 'full potential effect' of afforestation (ΔT_{p2})

139   derived by hypothesizing a transition from 100% complete openland coverage to 100%

140   complete forest coverage.

141

2 Methods

143   2.1 Three Approaches to Quantifying the Impacts of Afforestation on LST


144
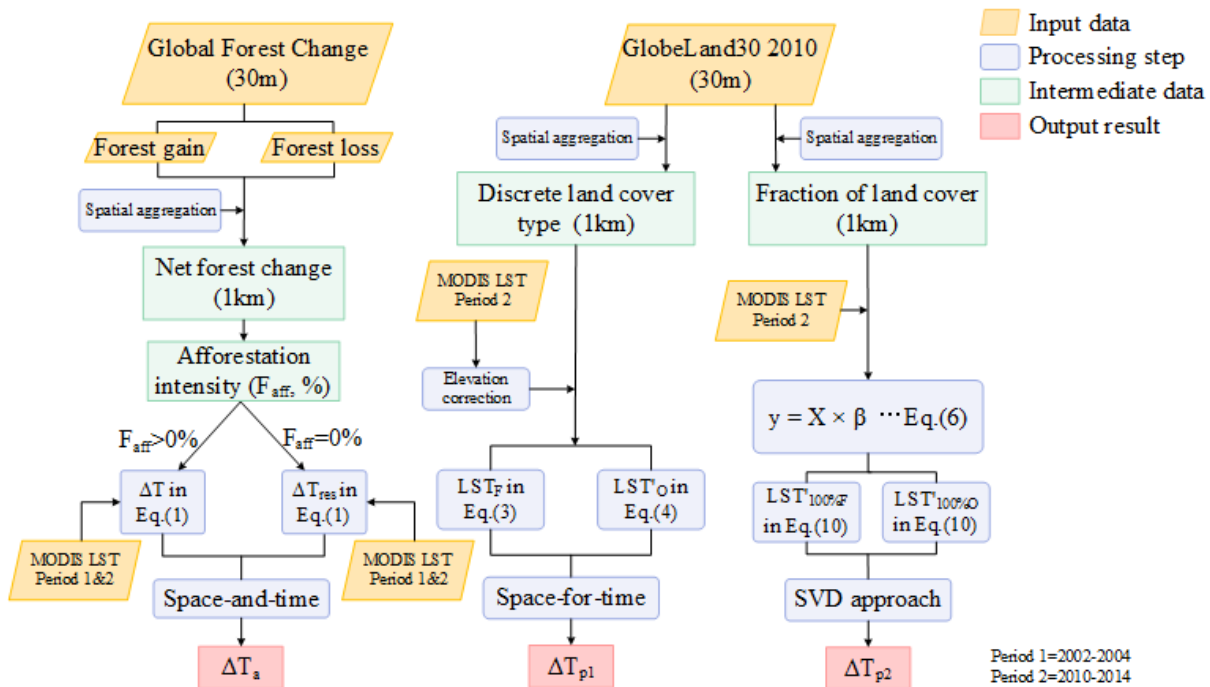
145   **Figure 2.** Schematic overview of the processing steps. The different output results correspond

146   to actual effect (ΔT_a), mixed potential effect (ΔT_{p1}) and full potential effect of afforestation

147   (ΔT_{p2}).

148

149   2.1.1 Actual Effect of Afforestation (ΔT_a)

150

151   The 'space-and-time' approach assumes that the gross change in land surface temperature (ΔT)

152   over a given time period during which afforestation occurred, contains both signals of

153   temperature change due to afforestation (ΔT_a) and background temperature variation (ΔT_{res})

154   due to changes in large-scale circulation patterns (Alkama and Cescatti, 2016; Li et al., 2016a):

7

$$\Delta T = \Delta T_a + \Delta T_{res} \tag{1}$$

where ΔT is the gross temperature change during the period from t_1 to t_2 for the pixel under study. ΔT can be calculated as the difference between LST_{t2} and LST_{t1}, with LST_{t2} being the surface temperature after afforestation and LST_{t1} being that before afforestation. It thus follows that

$$\Delta T_a = \Delta T - \Delta T_{res} \tag{2}$$

ΔT_{res} can be approximated by averaging changes in surface temperature for those pixels adjacent to the target afforestation pixel for which the forest cover remained constant between t_1 and t_2 (i.e., $F_{aff} = 0\%$; section 2.2.2). Here, pixels with $F_{aff} > 0\%$ were defined as afforestation target pixels. A searching window of 11 km by 11 km was established, centered on the afforestation pixel. Within this window, pixels with $F_{aff} = 0\%$ were defined as control pixels and were used to derive ΔT_{res}. Afforestation pixels and adjacent control pixels were both determined based on the net forest change between t_1 and t_2 using Global Forest Change (GFC) data (Fig. 2; Section 2.2.2).

2.1.2 Mixed Potential Effect (ΔT_{p1})

The 'space-for-time' method relies on the 'space-substitute-for-time' assumption to obtain the potential impact of afforestation on local temperature (Zhao and Jackson, 2014). By assuming that forest and openland share the same environmental conditions (background climate, topography, etc.) within a small spatial domain, the potential temperature effect of afforestation is examined using the search window method with a window size of up to 40km×40km (Ge et al., 2019; Li et al., 2015; Peng et al., 2014). Here, to be consistent with our 'actual effect' approach, a more conservative window size of 11km×11km was used, smaller than that used in the majority of previous studies (Ge et al., 2019; Li et al., 2015; Peng et al., 2014). In most

180   previous studies, existing medium resolution (1km) land-cover maps were used directly. Such

181   land-cover products rely on certain thresholds to classify satellite pixels into discrete land-cover

182   types. Given the widespread spatial heterogeneity in land-cover distribution, it is to be expected

183   that only in rare cases will these medium-resolution pixels have 100% coverage of a given land-

184   cover type. Therefore, when determined in this way, the potential effect of afforestation has

185   been named the 'mixed potential effect', in contrast to the 'full potential effect', on which we

186   will focus in the next section, which assumes a potential transition between land-cover types of

187   100% coverage.

188

189   To ensure consistency with the land-cover data used in the 'full potential effect' approach (i.e.,

190   the SVD method), the GlobeLand30 land-cover map was aggregated from its original resolution

191   (30m) to 1km resolution. The land-cover type assigned to a given 1km pixel during aggregation

192   was based on the land-cover type with an area fraction >50% within that pixel, to be consistent

193   with the rationale behind the generation of medium-resolution land-cover products (Section

194   2.2.2). A 1km forest pixel was then chosen as the target pixel and put at the center of a search

195   window with dimensions 11km×11km. The 'mixed potential effect' of afforestation (ΔT_{p1}) was

196   defined as the difference between the temperature of the target pixel (LST_F) and the average

197   temperature of all the surrounding openland pixels within the window ($\overline{LST_O'}$):

198                                    $$\Delta T_{p1} = LST_F - \overline{LST_O'} \qquad\qquad (3)$$

199   where LST_F is the surface temperature of the target forest pixel at t_2, and LST_O' represents the

200   elevation-corrected surface temperature of openland pixels at t_2 within the search window.

201   Given our search window size, ΔT_{p1} could be biased by the elevation difference between the

202   target forest pixel and surrounding openland pixels. Therefore, a linear relationship was first

203   fitted between the observed openland temperature, LST_O, and the elevation of the openland

204   pixel (Ele$_O$). This fitted temperature lapse rate was then used to derive elevation-corrected

205   openland temperature LST_O':

206                              $$LST_O' = LST_O + k \times \Delta Ele_{F-O} \qquad (4)$$

207   where ΔEle_{F-O} is the elevation difference between forest and openland pixels. The elevation is

208   available   from   NASA's   Shuttle   Radar   Topography   Mission   (SRTM)   data

209   (https://lpdaac.usgs.gov/products/srtmgl1v003/).

210

211   2.1.3 Full Potential Effect (ΔT_{p2})

212

213   The full potential effect represents the temperature change due to hypothesizing a shift from

214   100% openland to 100% forest coverage, and was determined here by employing the singular

215   value decomposition (SVD) method used in Duveiller et al. (2018). The SVD technique

216   assumes that the temperature observed for a pixel at 1km scale is a linear composition of the

217   temperatures of different land-cover types at a finer resolution (in our study at a 30m resolution).

218   For each 1km pixel, the observed temperature can be written as the composition of the

219   temperature of each component land-cover type and its corresponding fraction, based on the

220   land-cover fractions derived from the 30m-resolution GlobeLand30 map (Section 2.2). The

221   temperature of each type of land cover was assumed constant within a search window of 11km

222    $\times$ 11km. For each given search window, the following equations can be obtained:

223           $$\begin{pmatrix} y_1 \\ \vdots \\ y_n \end{pmatrix} = \begin{pmatrix} x_{11} & \cdots & x_{1m} \\ \vdots & \ddots & \vdots \\ x_{n1} & \cdots & x_{nm} \end{pmatrix} \times \begin{pmatrix} \beta_1 \\ \vdots \\ \beta_m \end{pmatrix} \qquad (5)$$

224   where n is the total number of 1km pixels within the window, after accounting for the elevation

225   difference (thus the maximum value of n is 121 given our 11km $\times$ 11km search window), m is

226   the number of land-cover types, x_{ij} refers to the fraction of land-cover type j in pixel i, β_i refers

227   to the temperature of land cover type i. To minimize elevation impacts, the linear regression

228   relationship for a given 1km pixel was included only when the elevation difference between

229   this pixel and the central pixel of the search window was smaller than 100m. Using matrix

230   notation, Eq. (5) can be simplified to:

231
$$y = X \times \beta \tag{6}$$

232   where the matrix X contains land-cover fraction for the n 1km pixels as an explanatory variable,

233   the response variable y contains n LST observations, and the coefficient vector, β, contains the

234   regression coefficients which show temperatures of different land-cover types. Note that this

235   linear equation system cannot be easily solved because the matrix X is 'closed', i.e., by

236   definition, the elements in each row of the matrix X add to 1. After removing the mean of each

237   column (Zhang et al., 2007), the matrix X was transformed, by applying the SVD technique, to

238   another matrix, Z, of reduced dimension (more details in Duveiller et al., 2018). After this

239   transformation, we have the following:

240
$$y = Z \times \beta' + \varepsilon \tag{7}$$

241   in which the β' coefficient can be obtained from equation (8):

242
$$\beta' = \left(Z^t Z \right)^{-1} Z^t y \tag{8}$$

243   However, the β' vector calculated from the transformed matrix Z cannot directly provide

244   surface temperatures for corresponding land-cover types. To obtain temperatures for each land-

245   cover type by assuming 100% ground coverage, an identity matrix Y with its dimension equal

246   to the number of land-cover types must be constructed to represent the hypothetical case in

247   which each 1km pixel was 100% covered by a single land-cover type. The same transformation

248   as applied to the matrix X was then applied to Y, to obtain a transformed matrix Z'. Finally, the

249   predicted temperature ($LST'_{100\%}$) for each land-cover type assuming a 100% coverage is

250   calculated as:

251 $$\mathrm{LST}^{'}_{100\%} = \mathrm{Z}^{'}\beta^{'} \tag{9}$$

252 For the central pixel of the local search window, $\Delta\mathrm{T}_{p2}$ is defined as the difference between the

253 predicted $\mathrm{LST}^{'}_{100\%}$ for forest ($\mathrm{LST}^{'}_{100\%F}$) and openland ($\mathrm{LST}^{'}_{100\%O}$).

254 $$\Delta\mathrm{T}_{p2} = \mathrm{LST}^{'}_{100\%F} - \mathrm{LST}^{'}_{100\%O} \tag{10}$$

255 More details, including an illustration of the SVD method, can be found in Fig. 7 in Duveiller

256 et al. (2018).

257

258 At the scale of the searching windows used in this analysis (11km×11km), any nonlocal effects

259 cancel out when comparing temperature differences over neighboring areas because the effects

260 of advection and atmospheric circulation have been reported to be similar for adjacent areas

261 (Pongratz et al., 2021; Winckler et al., 2019a). Hence the quantified afforestation effect for each

262 of the three methods can be considered to be the local effect only.

263

264 ## 2.2 Dataset and Processing

265 2.2.1 The Test Case: Large-scale Afforestation over China

266

267 China was selected as the test case for addressing the important methodological issues in

268 quantifying land surface impacts of afforestation because afforestation is a key national strategy

269 for sustainable development and climate mitigation (Bryan et al., 2018; Qi et al., 2013).

270 According to the 8th National Forest Inventory conducted in 2013, China's afforestation area

271 has reached 6.9×10^3 million ha, accounting for 33% of the total global afforestation area (Chen

272 et al., 2019). Afforestation in China during 2000–2012 occurred mainly in regions with more

273 than 400 mm of precipitation per year (Fig. 3a), which is considered a threshold below which

274 there is a high risk of afforestation failing due to water limitation (Mátyás et al., 2013). China

275 covers a wide range of latitude from 3.9° N to 53.6° N and its forest ecosystems cover an

276 elevation range of 100m to 4000m. This wide range of climate zones, from tropical/subtropical

277 to temperate and boreal, make it highly suitable for our methodological analysis because the

278 impact of afforestation on LST might differ with latitude and background climate (Lee et al.,

279 2011; Alkama and Cescatti, 2016). Further justification for using China as a test case comes

280 from the strongly diverging published LST impacts of afforestation there, which range from an

281 actual effect of -0.0036K decade^{-1} by Li et al. (2020) to a potential effect of -1.1K by Peng et

282 al. (2014).

283

284 2.2.2 MODIS Dataset and Preparation

285

286 In this study, the actual effect was estimated by combining the actual satellite-derived

287 afforestation for 2000 to 2012 (see Section 2.2.2) with satellite-based estimates of biophysical

288 variables for the periods 2002–2004 (t_1) and 2010–2014 (t_2). MODIS remote sensing products

289 for land surface temperature (MOD11A2), albedo (MCD43B3) and evapotranspiration

290 (MOD16A2) were used to characterize the biophysical effects (Table 1). The datasets were

291 regridded to harmonize with spatial (1km) and temporal (annual) resolutions (Table 1).

292

293 The MOD11A2 product provides 8-day land surface temperature for 10:30 AM and 22:30 PM

294 from the Terra satellite, but here we focused on daytime surface temperature. Only valid LST

295 observations from the original data were used to compute the average daily values for a given

296 year. Years for which more than 40% of daily data are missing were excluded from the analysis.

297 Annual data were then aggregated to obtain the average annual temperature for periods t_1 and

298 t_2.

299

300   The MCD43B3 product provides white-sky and black-sky shortwave albedo at 16-day temporal

301   resolution (Table1). The observed white-sky albedo was used as the daytime albedo (Peng et

302   al., 2014). For evapotranspiration (ET), we used the ET band in MOD16A2, which includes

303   water fluxes from soil evaporation, wet canopy evaporation and plant transpiration. To calculate

304   the mean annual albedo and evapotranspiration for 2002–2004 (t_1) and 2010–2014 (t_2) we used

305   the same approach as used for LST.

306

307   2.2.3 Land-Cover Datasets and Processing

308

309   Two land-cover datasets were used in this study: the 'actual effect' approach was based on the

310   Global Forest Change (GFC) dataset, while the 'mixed potential effect' and 'full potential effect'

311   used the GlobeLand30 land-cover data (Table 1).

312

313   The SVD technique, used in the 'full potential effect' approach, requires a land-cover map with

314   a higher spatial resolution than the 1km spatial resolution of the LST data. The GlobeLand30

315   product, which is based on Landsat images, provides land-cover information for China at a 30m

316   resolution for the years 2000 and 2010 (Chen et al., 2015). Cultivated land and grassland in

317   GlobeLand30 were classified as openland. Discrete land-cover type information at 30m

318   resolution in 2010 was aggregated to obtain the area fractions of the different land-cover types

319   at 1km resolution, which were then used to construct matrix X in Eq. (5) (Fig. 2). Furthermore,

320   land-cover type information at the 1km scale was extracted, based on the vegetation type with

321   area fraction >50% for every 1km×1km window. This data was then applied in the 'space-for-

322   time' method to identify forest and openland (Fig. 2).

323

324 GlobeLand30 data is not suitable for detecting forest change (Zeng et al., 2021). The Global

325 Forest Change (GFC) data, however, provides forest gain and forest loss at a spatial resolution

326 of 30m between 2000 and 2012 and has been used for mapping global forest change (Hansen

327 et al., 2013). This product shows an overall accuracy of greater than 99% for areas of forest

328 gain at the global scale when compared with statistical data reported in Forest Resource

329 Assessment (FRA), LiDAR detection (Geoscience Laser Altimetry System), and MODIS

330 NDVI time series (Hansen et al., 2013), and thus has been recommended for use in forest and

331 forest-change estimates (Chen et al., 2020; Zeng et al., 2021). Using this dataset, forest loss

332 events were identified for each year between 2000 and 2012, but forest gain was only identified

333 for the whole period, simply because forest loss is an abrupt change which can be effectively

334 identified over short time periods, whereas forest gain is a gradual change which can only be

335 confidently identified over longer time spans. Here, forest losses and gains from GFC were

336 aggregated at a 1km resolution to obtain net forest change (defined as forest gain minus forest

337 loss) during this period (Fig. 2). A positive net change indicates afforestation and the area

338 percentage of afforestation for the 1km pixel area was defined as F_{aff}. The land-cover type of

339 pixels with $F_{aff} = 0\%$ was considered to be stable. This net forest-change information was then

340 used in the calculation of the actual afforestation-induced temperature effect (ΔT_a)(Fig. 2).

341

342 2.3 Decomposition of Changes in Surface Temperature

343

344 Changes in surface temperature following forest-cover change are the net result of changes in

345 underlying fluxes that collectively determine the land surface energy balance:

346 $$\Delta SW_{in} - \Delta SW_{out} + \Delta LW_{in} - \Delta LW_{out} = \Delta H + \Delta LE + \Delta G \qquad (11)$$

347 where ΔSW_{in}, ΔSW_{out}, ΔLW_{in}, ΔLW_{out} are the changes in incoming and outgoing shortwave

348 and longwave radiation, respectively, and ΔH, ΔLE, and ΔG are changes in sensible heat flux,

15

349 latent heat flux and ground heat flux, respectively. All the terms of Eq. (11) are expressed in

350 Wm^{-2}.

351

352 Firstly, it can be reasonably assumed that $\Delta SW_{in} \approx 0$ and $\Delta LW_{in} \approx 0$, given that all three

353 approaches consider only local effects on surface temperature by following a comparison of

354 target pixels with surrounding control pixels, thus excluding feedbacks from, e.g., cloud

355 formation (Duveiller et al., 2018). Changes in reflected shortwave radiation can be derived as:

356 $$\Delta SW_{out} = SW_{in} \times \Delta\alpha \qquad (12)$$

357 where SW_{in} is available from the CERES EBAF-Surface Product Ed 4.1 (Kato et al., 2018; Liu

358 et al., 2018) (Table 1), and $\Delta\alpha$ is the surface albedo change. To approximate ΔLW_{out}, we used

359 its first order differential equation:

360 $$\Delta LW_{out} = \sigma(4\varepsilon_B T^3 \Delta T + \Delta\varepsilon_B T^4) \qquad (13)$$

361 where σ is Stefan-Boltzmann's constant (5.67×10^{-8} W m^{-2} K^{-4}), T is daytime surface

362 temperature and ΔT is the afforestation impact on surface temperature. Surface broadband

363 emissivity, ε_B, is usually obtained from an empirical relationship (Zhang et al., 2019):

364 $$\varepsilon_B = 0.2122\varepsilon_{29} + 0.3859\varepsilon_{31} + 0.4029\varepsilon_{32} \qquad (14)$$

365 where ε_{29}, ε_{31} and ε_{32} are obtained from the estimated emissivity for bands 29 (8,400–8,700 nm),

366 31 (10,780–11,280 nm) and 32 (11,770–12,270 nm) in the MOD11C3 data (Duveiller et al.,

367 2018).

368

369 Latent heat flux change (ΔLE) refers to changes in the energy used for evapotranspiration (ET,

370 unit: mm d^{-1}), which can be obtained from the change in evapotranspiration (ΔET):

371 $$\Delta LE = \Delta ET \times 28.94 \text{ W m}^{-2}/(\text{mm d}^{-1}) \qquad (15)$$

372 Therefore, the sum of sensible heat change and ground heat change ($\Delta H + \Delta G$) can be calculated

373 as the difference between net radiation change and latent heat flux change (ΔLE) based on Eq.

374   (11). The afforestation effects on albedo ($\Delta\alpha$), ε_B ($\Delta\varepsilon_B$) and ET (ΔET) needed in the above

375   equations were calculated in a similar way to ΔT for each of the three different approaches as

376   described in Section 2.1.

377

378   2.4 Statistical Analysis

379   The spatial distributions of original samples for the three methods are different because of the

380   different land-cover maps used (Fig. 2 and Figure A1) and, therefore, the statistical analysis

381   was limited to those pixels shared by all three approaches: 96,058 sample pixels at 1km

382   resolution. The distribution of these shared sample pixels retained the characteristics of the

383   spatial distribution of the original samples (Figure A2).

384

385   Differences in the afforestation effects on LST of the three approaches were tested by

386   performing paired-samples *t*-tests between pairs of approaches. The paired-samples *t*-test was

387   used, rather than a normal *t*-test, to avoid the bias due to strong spatial heterogeneity in the LST

388   effects of afforestation that could occur if the values of all pixels had been pooled together for

389   a normal *t*-test. The test was made using the 'ttest_rel' method from the 'scipy.stats' package

390   in Python. The Bonferroni correction was applied to adjust the significance level (p-value) to

391   mitigate the increasing Type I error when making multiple paired-samples *t*-test, which in our

392   case involves three pairs (Lee and Lee, 2018; UC Berkely, 2008). The Bonferroni correction

393   sets the significance cut-off at α/k (with α as the p-value before correction and k as number of

394   pairs). In this study, with 3 hypotheses tests (i.e., 3 pairs) and an original significance level $\alpha =$

395   0.05, the adjusted p-value is 0.0167. In order to investigate ΔT_a in relation to the afforestation

396   intensity, a linear regression was performed between ΔT_a and F_{aff} using the ordinary least

397   squares method.

398

17

399   Table 1 Summary of the datasets and their main characteristics

Type	Dataset	Selected band	Resolution	Projection	Timespan
Forest change	Global Forest Change	Forest gain; Loss year	30m, annual	WGS84	2000–2012
Land-cover type	GlobeLand 30	Land-cover type	30m, —	UTM	2000; 2010
Land surface Temperature	MOD11A2	Daytime temperature	1km, 8days	sinusoidal	2002–2004; 2010–2014
Albedo	MCD43B3	Albedo WSA shortwave	1km, 16days	sinusoidal	2002–2004; 2010–2014
Incoming shortwave radiation	CERES	sfc_sw_down_all_mon	1°, monthly	WGS84	2002–2004; 2010–2014
Surface broadband emissivity	MOD11C3	Emis_29; Emis_31; Emis_32	0.05°, monthly	sinusoidal	2002–2004; 2010–2014
Evapotranspiration	MOD16A2	ET_500m	500m, 8days	sinusoidal	2002–2004; 2010–2014
Elevation	SRTM30	Be75	30m, —	WGS84	—

400

3 Results

3.1 Spatial Distribution of Afforestation and its Effect on Land Surface Temperature

In China, afforestation areas are mainly located in the northeast, southwest and south, where sufficient precipitation is available (Fig. 3a) and largely driven by afforestation of former cropland or abandoned cropland, with a relatively small contribution from forest regeneration or replanting following natural disturbance or timber harvest. One prominent feature of afforestation in China is its small afforestation patch, with most afforested pixels ($1km^2$) having an afforestation fraction of less than 30% (Fig. 3b). Pixels with an afforestation intensity below 10% account for 93% of the total number of pixels (Fig. 3b), representing 0.14 Mha, more than half (55.6%) of the total afforestation area (Fig. 3b).
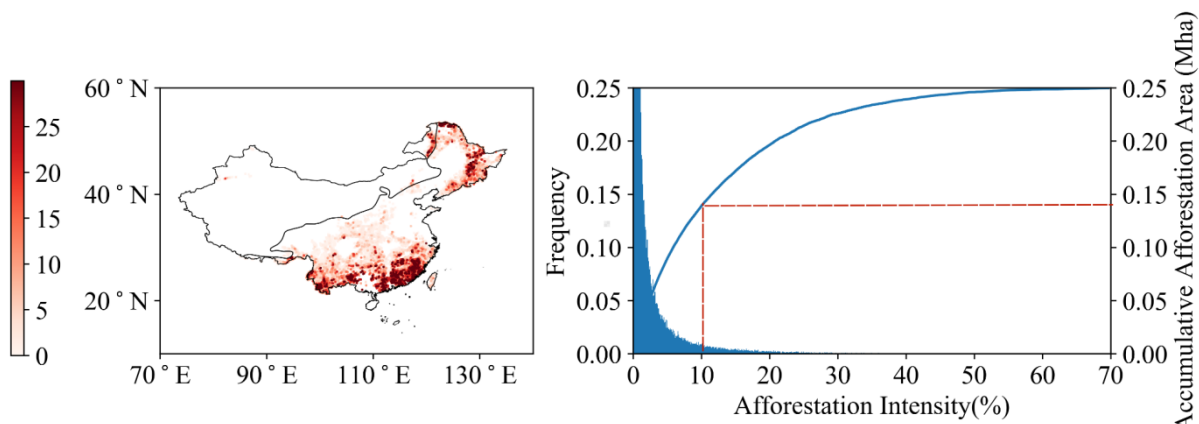
Figure 3. (a) Spatial distribution of afforestation intensity (F_{aff}) in China during 2000–2012. The solid black line crossing China is the 400mm annual precipitation isoline. (b) Frequency distribution of F_{aff} and cumulative afforestation area with the increase in F_{aff}. The red dashed line represents the cumulative afforestation area corresponding to $F_{aff} = 10\%$.

419   Although all three approaches result in similar spatial and latitudinal patterns regarding

420   afforestation effects on LST (Fig. 4), their magnitudes differ substantially. The actual effect has

421   the lowest temperature change, followed by the mixed potential effect, with the full potential

422   effect showing the greatest temperature change (Fig. 4a–c). For the latitude range of 20–36° N

423   where afforestation effects show a dominant cooling effect, the full potential effect (ΔT_{p2})

424   reaches -1.75±0.01K, while the mixed potential effect (ΔT_{p1}) was smaller at -0.96±0.00K, but

425   both of them were much larger than the actual effect (ΔT_a) of -0.09±0.00K. Similarly, the full

426   potential effect (ΔT_{p2}) showed the strongest warming effect (0.35±0.01K) in the area north of

427   48° N, stronger than the mixed potential effect (0.22±0.01K), and again the actual effect is the

428   smallest (0.07±0.01K). However, regarding the latitude where the effects change from a

429   warming to cooling effect, the three approaches largely converge (Fig. 4d). Between 40° N and

430   48° N, the afforestation effects are largely neutral, with the mean temperature change for the

431   three approaches being 0.07±0.01K (ΔT_a=-0.01±0.01K; ΔT_{p1}=0.11±0.01K; ΔT_{p2}=0.12±0.01K).
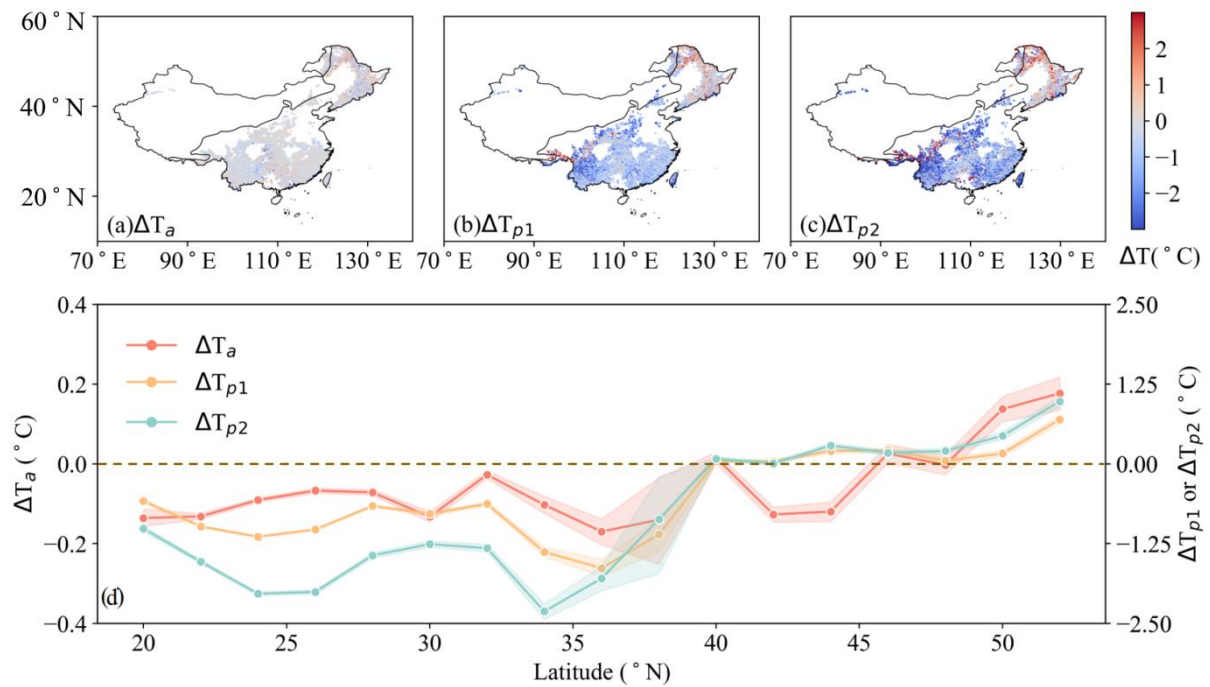
432

433   **Figure 4.** Afforestation effects on LST quantified by three approaches: (a) actual effect based

434   on a 'space-and-time' approach (ΔT_a), (b) mixed potential effect based on a 'space-for-time'

20

approach (ΔT_{p1}) and (c) full potential effect assuming a transition from 100% openland

coverage to 100% forest coverage using the SVD method (ΔT_{p2}). The solid black line crossing

China is the 400mm precipitation isoline. (d) Zonal averages of the annual mean daytime LST

change within 2° latitudinal bins, with shaded areas representing the standard errors (SE). Note

that in panel (d), ΔT_a corresponds to the vertical axis on the left; ΔT_{p1} and ΔT_{p2} correspond to

the vertical axis on the right.

3.2 Reconciling Temperature Effects of Afforestation

Even though the observed land surface temperature is assumed to be uniform for the 1km

afforested satellite pixel, the underlying afforestation intensity varies substantially (Fig. 3a).

This leads to our first hypothesis that for a 1km pixel, ΔT_a should be influenced by the area

fraction that has been afforested within the pixel (i.e., afforestation intensity or F_{aff}). Indeed, the

actual daytime surface cooling increases significantly with afforestation intensity (Fig. 5), with

a 0.079±0.017K (mean ± std) increase for each ten percent increase in F_{aff}.
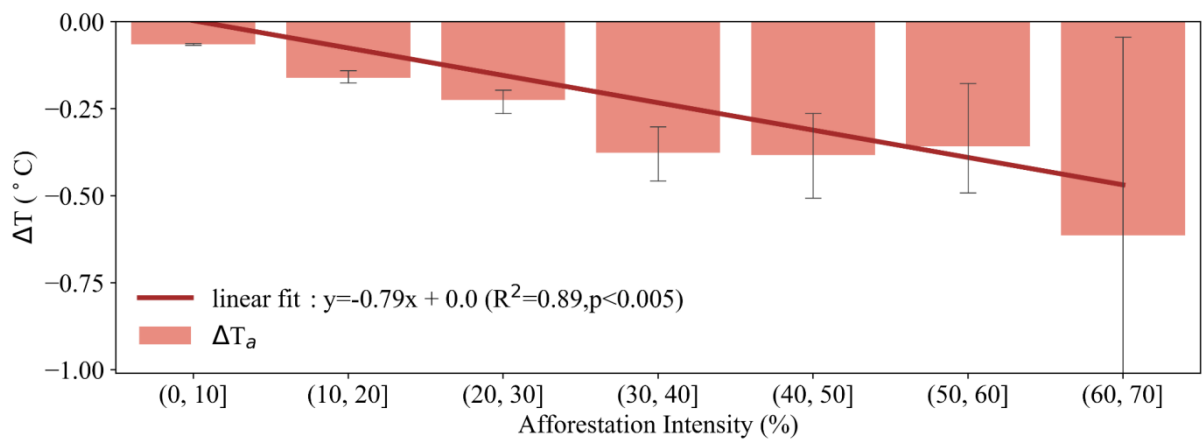
Figure 5. Changes in ΔT_a as a function of afforestation intensity (F_{aff}), defined as the fraction

of afforested area to the total pixel area at a 1-km resolution. Error bars indicate the standard

error of ΔT_a within each ten percent bin of F_{aff}. The red line represents the fitted linear

regression line between ΔT_a and F_{aff}.

455

456 The afforestation effects obtained from the three approaches were compared for each F_{aff}

457 interval (Fig. 6). When afforestation intensity is less than 60%, significant differences exist in

458 the temperature change obtained by the three approaches, with $\Delta T_a < \Delta T_{p1} < \Delta T_{p2}$. This result

459 confirms our second hypothesis that the actual effect is expected to be smaller than potential

460 effects. However, for pixels with relatively low F_{aff}, the mixed potential effect is found to be

461 smaller than the full potential effect, which is reasonable, but to our knowledge, has not been

462 reported before. When the afforestation intensity is greater than 60%, the significant difference

463 in cooling effect between the different approaches disappears, likely because afforestation

464 intensity, and the associated forest coverage at 1km resolution, reach values high enough to

465 allow the 'potential' effects to be realized.
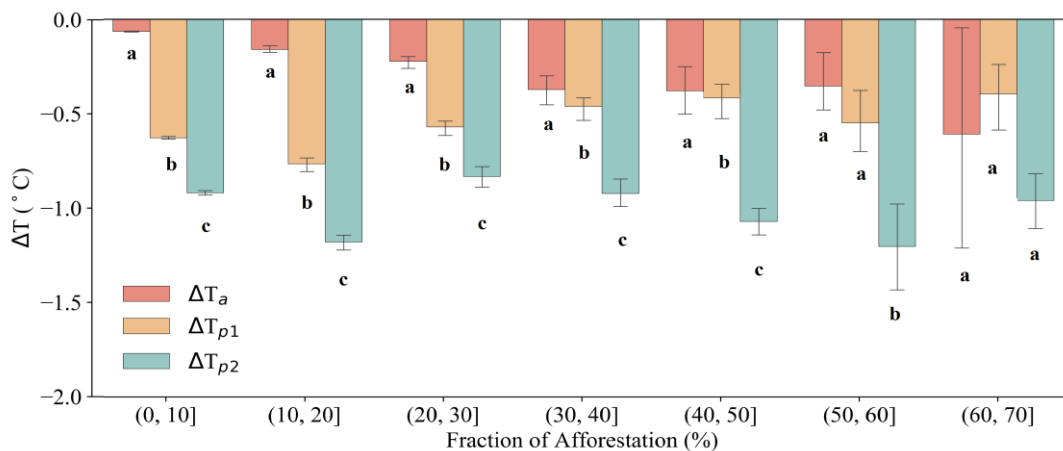
466 **Figure 6.** Comparison of ΔT for the three approaches for bins of afforestation intensity. Error

467 bars are given as the standard error and different letters indicate that ΔT calculated by the two

468 approaches concerned are significantly different using the adjusted p-value after applying the

469 Bonferroni correction for multiple paired-samples *t*-tests.

470

471 When considering the overall differences in ΔT for the three approaches, irrespective of the

472 afforestation intensity, ΔT_a (-0.07±0.00K) over China was significantly lower than ΔT_{p1} (-

473 0.63±0.00K), which is further significantly lower than ΔT_{p2} (-1.16±0.01K) ($p < 0.05$, paired-

474   samples t-test, n= 96,058), once again confirming our second hypothesis (Fig. 7). Moreover,

475   extrapolation of the relationship shown in Fig. 5 suggests that ΔT_a would reach -0.79±0.17K

476   (mean ± std) if a 1km pixel was 100% afforested, which is conceptually comparable to the

477   potential effects. ΔT_a was indeed found to be higher than ΔT_{p1} but lower than ΔT_{p2}. This result

478   confirms our third hypothesis and demonstrates that the potential cooling effect could indeed

479   be reached when a pixel is fully afforested.

480
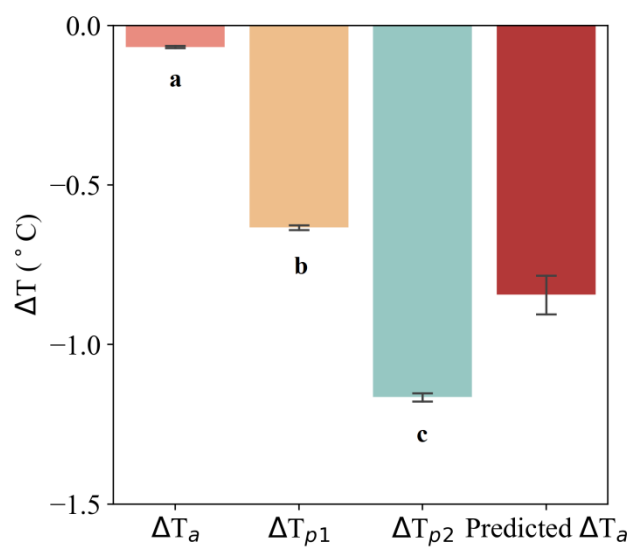
481   **Figure 7**. Comparison of ΔT for the three approaches, irrespective of the afforestation intensity.

482   Error bars are given as the standard error and different letters indicate ΔT being significantly

483   different (p = 0.0167, paired-samples t-test, n = 96,058). For comparison, the predicted ΔT_a

484   with F_{aff} reaching 100%, which is conceptually comparable with ΔT_{p1} and ΔT_{p2}, is also shown.

485

486   3.3 Reconciling Changes in Surface Energy Fluxes by Afforestation

487

488   In order to investigate whether the underlying surface energy fluxes could be reconciled

489   following the reconciliation of the LST changes, changes in surface energy fluxes due to

490   afforestation were quantified using each of the three approaches, under the same boundary

conditions as for full afforestation (i.e., changes following the 'actual effect' approach were extended for F_{aff} = 100%). As illustrated in Fig. 8, changes in all the relevant surface energy fluxes under the three different approaches have the same direction, with similar magnitudes, confirming the reconciliation of the different approaches in terms of surface energy fluxes. More specifically, the three approaches converge on a reduction in reflected shortwave radiation (ΔSW_{out}) of 0.56~1.23 W m^{-2} due to the lower albedo of forest compared to openland (Figure A3). Emitted longwave radiation (ΔLW_{out}) was reduced by 1.03~3.10 W m^{-2} and sensible and ground heat fluxes ($\Delta H + \Delta G$) reduced by 4.84~6.14 W m^{-2}. All these reduced fluxes were offset by an increased latent heat flux of 7.99~8.41 W m^{-2} (ΔLE), the single energy flux leading to surface cooling.
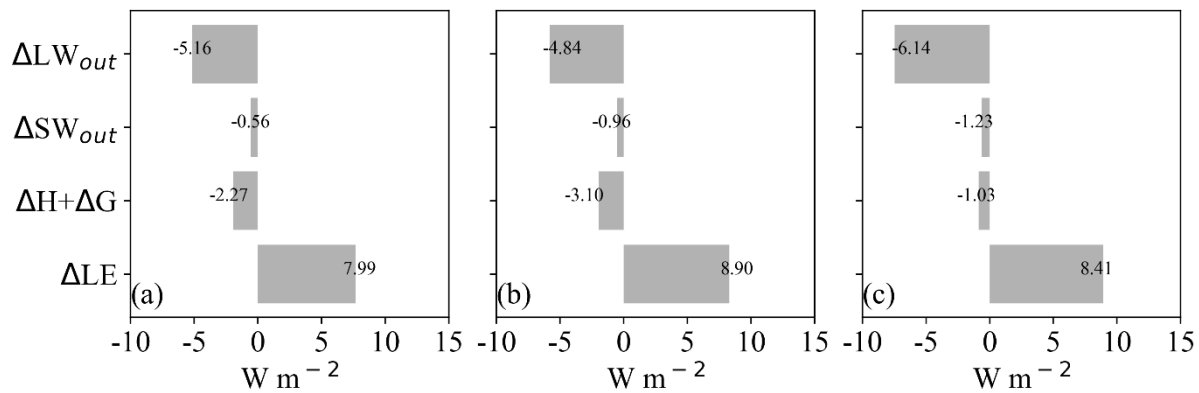
Figure 8. Afforestation-induced changes in surface energy fluxes (Wm^{-2}) following the three approaches: (a) actual effect based on a 'space-and-time' approach, (b) mixed potential effect using medium-resolution land cover maps based on a 'space-for-time' approach and (c) full potential effect assuming a transition from 100% openland coverage to 100% forest coverage using the SVD method. For each approach, changes were calculated for the reflected shortwave radiation (SW$_{out}$), outgoing longwave radiation (LW$_{out}$), latent heat flux (LE) and the combination of sensible and ground heat fluxes (H+G). No changes were assumed for incoming shortwave and longwave radiation. Changes in energy fluxes for the 'actual effect' approach have been adjusted to the condition of full afforestation (i.e., F_{aff} = 100%) in a similar way as

24

511   for the 'predicted ΔT_a' in Fig. 7, by fitting linear regressions between energy flux variables and

512   F_{aff} (Figure A4).

513

514   4 Discussion

515

516   The three approaches (Li et al., 2015; Alkama and Cescatti, 2016; Duveiller et al., 2018) used

517   to quantify local surface temperature change following forest-cover change and presented with

518   details in this study, have been cited over 919 times in research papers (Web of Science,

519   December 2021) and in high-level climate science synthesis reports. Despite the apparently

520   large differences in temperature effect among them, to our knowledge, no studies have

521   examined whether these differences can be reconciled. This study fills that gap by comparing

522   the three approaches for a single study case, i.e., large-scale afforestation in China. China is

523   highly suitable for the purpose of this study as the size of an afforestation patch is, in general,

524   smaller than the spatial resolution (1km) at which the temperature effects of afforestation were

525   conducted in the previous studies describing the three approaches (Li et al., 2015; Alkama and

526   Cescatti, 2016; Duveiller et al., 2018). Hence, the difference between the actual and potential

527   temperature effects is expected to be large.

528

529   Indeed, we found surface cooling following afforestation was much less when estimated as the

530   actual effect (ΔT_a) compared to the potential effects (ΔT_{p1} and ΔT_{p2}). This lower ΔT_a has been

531   attributed to incomplete afforestation at a 1km resolution, at which potential effects are

532   quantified by assuming complete afforestation (i.e., a complete shift from openland to forest).

533   Consistent with our first hypothesis, the afforestation fraction at a 1km resolution explained 89%

534   of the variation in ΔT_a, making it a key determinant of the surface cooling following

535   afforestation (Fig. 5). This result is consistent with the fact that the observed temperature for a

mixed surface is determined by the area fractions of its respective components, with each component having a unique temperature. This fact also forms the theoretical foundation for the SVD technique used to derive the full potential effect (Duveiller et al., 2018).

Modelling (Li et al., 2016b) and satellite-based (Alkama and Cescatti, 2016) studies have found that temperature change after afforestation (or deforestation) is highly sensitive to the fraction of the model grid cell or satellite pixel that is subjected to afforestation (or deforestation), echoing our finding that ΔT_a significantly changes with F_{aff}. In addition, we provide strong evidence in support of our third hypothesis that when F_{aff} reaches 100%, the expected actual effect is comparable to the potential effects (Fig. 7). This finding shows that the three approaches compared here are consistent when the same boundary condition, i.e., full afforestation, is applied, and demonstrates that all three methods are mutually compatible. It is, therefore, the basis of the reconciliation of the three approaches. It also highlights the fact that the actual afforestation area must be considered when evaluating the climate mitigation effects of afforestation.

Our results also show that the mixed potential effect (ΔT_{p1}) is smaller than the full potential effect (ΔT_{p2}) (Fig. 6, Fig. 7). We suspect that this phenomenon likely also relates to the incomplete forest coverage for the identified forest pixels at the 1km scale used in the 'space-for-time' analysis, because a threshold value of 50% forest cover was used when upscaling the 30m land-cover map to 1km resolution. This threshold, however, is consistent with the commonly applied value in land-cover classification based on medium resolution satellite images, such as MCD12Q1, which uses a tree coverage value of 60% to identify forest pixels (Sulla-Menashe and Friedl, 2018). For the purpose of comparison, we also calculated the mixed potential effect based on the MCD12Q1 land-cover map but using the same LST data. The

result shows that potential effects derived using MCD12Q1 data versus those derived using spatially upscaled GlobeLand30 data are almost identical (Figure A5), lending credibility to our estimated ΔT_{p1} in comparison to previous studies using MODIS land-cover data (Li et al., 2015). Progressively increasing the forest-cover threshold from 50% to 90% steadily increases ΔT_{p1} from -0.62±0.02K to -0.75±0.02K (Figure A6). Further increasing the thresholds used to identify 1km-resolution openland pixels from 50% to 90% increases ΔT_{p1} from -0.63±0.00K to -1.10±0.02K (Figure A7), bringing ΔT_{p1} even closer to ΔT_{p2} (-1.16±0.01K). This is consistent with the finding of a previous study on the dependence of the temperature effect on the forest cover change thresholds that were used to define afforestation: the higher the threshold, the stronger the impact on temperature (Li et al., 2016). Our results add further support to the compatibility of the three approaches given the same boundary condition, i.e., the complete transformation from full openland to full forest coverage.

Several factors may contribute to the remaining differences in the temperature effects produced by different methods even after reconciliation. As described in the Method section, there are discrepancies in the assumptions of the three approaches, which lead to differences in the control pixels (i.e., adjacent comparison pixels). For instance, for the 'pure potential effect' it is assumed that the LSTs for pixels with the same land cover type are uniform and forest pixels are compared with openland pixels, whereas the in the 'mixed potential impact' approach the central target forest pixel is compared with the mean value of non-forest pixels within the searching window. Moreover, space-for-time is an assumption that cannot be verified (Chen et al., 2016), and which will inevitably result in differences in the estimated actual and potential effects, although the consistency between 'potential' and 'actual' effects after reconciliation in our study does illustrate the broad validity of this assumption.

Differences between the actual and potential temperature effects can also arise from the time period elapsed following afforestation. The temperature effect caused by deforestation is considered to be instant (Liu et al., 2018), while, in contrast, afforestation-driven surface temperature change depends on different stages of forest development and is expected to saturate only when the forest canopy stabilizes (Ziter et al., 2019). The GFC dataset used in this analysis defined forest gain using the condition of successful detection of a stable closed forest canopy that is clearly different from a non-forest state (Hansen et al., 2013), which enhances the chance of temperature change saturation following afforestation. But, given a maximum stand age of 12 years inferred from the GFC dataset, differences in surface temperatures may still exist between newly established forests and the mature existing forests that were used in the 'potential effect' approaches. Thus, we cannot exclude the possible contribution of such a mechanism to the difference between the actual and potential effects, which failed to be reconciled.

Previous analyses have documented latitudinal patterns of surface temperature change induced by afforestation (Alkama and Cescatti, 2016; Li et al., 2015, 2016a; Peng et al., 2014). When comparing the three approaches for a single case study, consistent latitudinal patterns of local surface temperature effects following afforestation are observed (Fig. 4). Notably, all three approaches show a warming effect in the northern high latitudes and an opposite cooling effect in the southern low latitudes, with a largely neutral effect in the 40–48° N latitude band, providing further evidence that the three approaches are compatible. In particular, although the three approaches used different land-cover maps, they derived consistent LST impacts following afforestation, which highlights that fact that the reconciliation provided in this study is rather robust and unlikely to be dependent on the land cover datasets used.

611   In addition to the reconciliation of the land surface temperature change, we checked and

612   confirmed that the changes in surface energy fluxes that underlie and drive the changes in

613   surface temperature are compatible under the boundary condition of full afforestation. This

614   finding confirms the inherent consistency in the three approaches and clarifies the reasons

615   behind the apparent discrepancies in existing studies as discussed in the introduction.

616   Nonetheless, when it comes to the biophysical impacts of afforestation in the real world, our

617   findings have far-reaching implications. Full afforestation is often possible at small spatial

618   scales but becomes challenging at large scale. Therefore, the realization of the full potential

619   effect by afforestation is scale-dependent. For example, a complete afforestation of the semi-

620   arid Loess Plateau in the northwest of China is predicted to generate a surface cooling effect of

621   2.40 ± 0.07K, but substantial afforestation efforts over the past 4 decades in that region have only

622   realized a cooling of 0.11 ± 0.01K as measured by the 'actual effect'. Because of greater water

623   consumption by forest compared to openland and the need to maintain land area for food

624   production, achieving the full cooling potential may not be feasible (Huang et al., 2018; Liu

625   and She, 2012; Liang et al., 2019).

626

627   Potential cooling effects have a value in that they can serve to establish the envelope of effects

628   and measure possible outcomes given the condition of full afforestation. However, given the

629   challenge of full afforestation at large spatial scales, potential effects should be converted into

630   a more realistic estimate (i.e., actual effects), by taking into account the intensity of afforestation,

631   to better represent policy ambitions. The analog could also be made for the effects of the surface

632   energy impacts of afforestation. Taking 10% as the afforestation intensity threshold to compare

633   the cumulative surface energy effect between the actual and potential approaches, actual

634   cumulative biophysical changes (5.06 EJ) for 2000–2012 are much smaller than mixed potential

635   changes (20.13 EJ) and full potential change (19.02 EJ) (methods in Text A1; Figure A8). Again,

this shows that simply using the potential effects for policy making or evaluation risks greatly overestimating the biophysical effects of afforestation.

5 Conclusions

In this study we provided a synthesis of the three influential methods used to quantify afforestation impact on surface temperature change and provided evidence that these different methods could in fact be reconciled. The actual effect of surface temperature change following afforestation was highly dependent on the intensity of afforestation (F_{aff}), which explained 89% of the variation in ΔT_a. With the common boundary condition of full afforestation being applied, differences in afforestation impacts on LST reported by the three methods in previous studies greatly reduced, showing that simply treating these differences as uncertainty is incorrect and could greatly overestimate the uncertainty. In other words, when full afforestation is assumed, the actual effect approaches the potential effect, demonstrating the effectiveness of the 'space-for-time' approach and that the potential cooling effect of afforestation could indeed be realized. Potential cooling effects have a value in academic studies where they can be used to establish an envelope of effects, but their realization at large scales is challenging given the scale dependency. The reconciliation of the different approaches demonstrated here stresses that the afforestation fraction should be accounted for in order to bridge different estimates of surface cooling effects in policy evaluation.

Appendix A
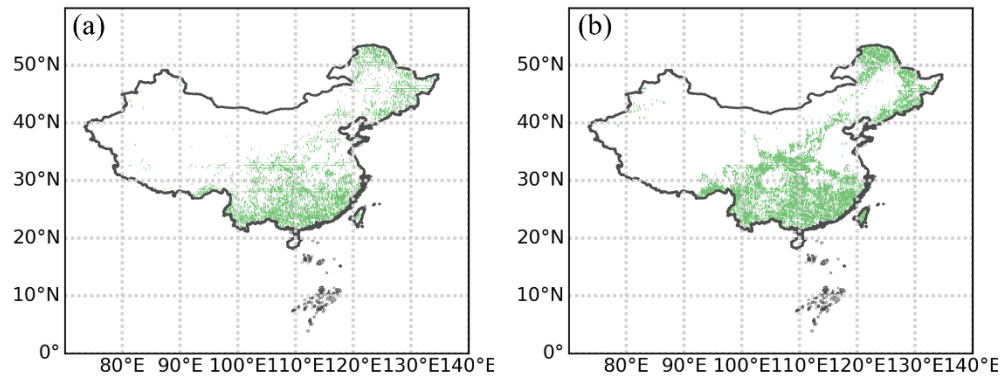
Figure A1. The distributions of the original sample pixels (at a 1km resolution) for (a) the

actual effect and (b) the two potential effects.
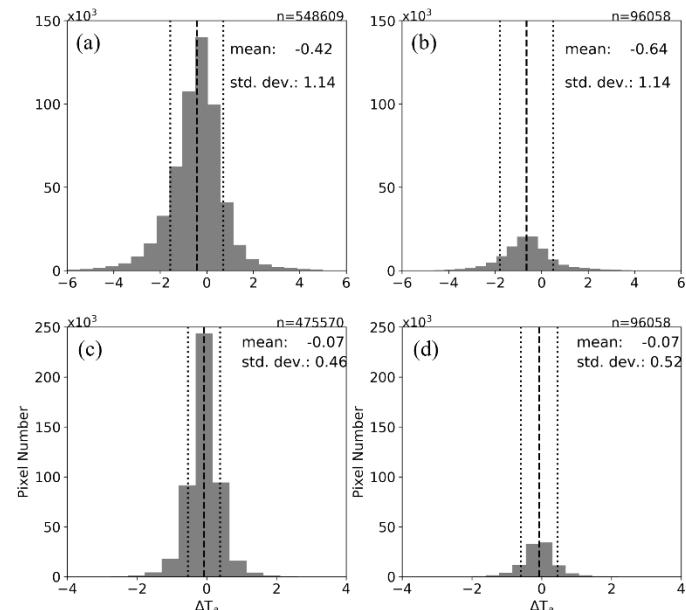
**Figure A2.** (a) Histogram of ΔT_a of all pixels based on the GFC dataset (b) Histogram of ΔT_a

for samples used for the statistical test. (c) Histogram of ΔT_{p1} of all pixels based on GFC dataset

(d) Histogram of ΔT_{p2} for samples used for the statistical test.
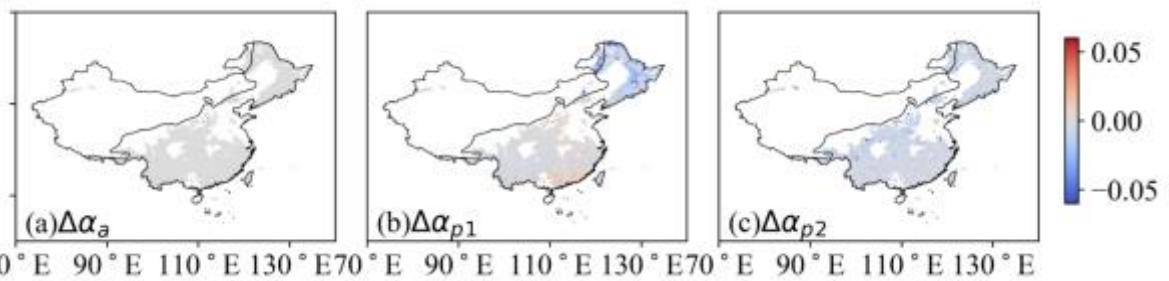
Figure A3. Spatial distribution of afforestation-induced changes in albedo (α) over China from three approaches: (a) Actual albedo change following afforestation based on 'space-and-time' method ($\Delta\alpha_a$), (b) mixed potential albedo change using medium-resolution land-cover maps based on 'space-for-time' approach ($\Delta\alpha_{p1}$) and (c) full potential effect ($\Delta\alpha_{p2}$) based on SVD approach.
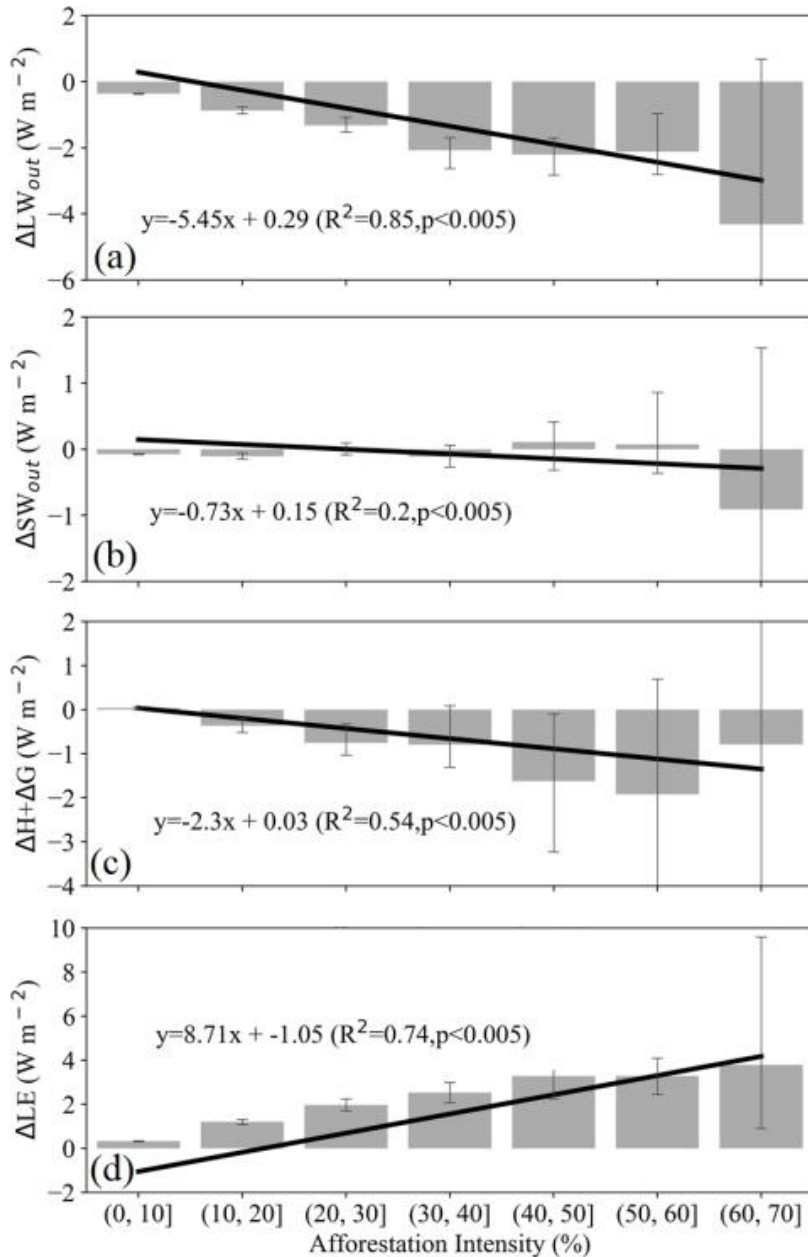
Figure A4. Changes of actual effect in (a) ΔLW, (b) ΔSW, (c) $\Delta H + \Delta G$ and (d) ΔLE (W m^{-2}) as a function of afforestation intensity (F_{aff}) following the 'actual effect' approach. Error bars indicate the standard error within each ten percent bin of F_{aff}. The solid black lines represent the fitted linear regression line between each energy flux variable and F_{aff}.
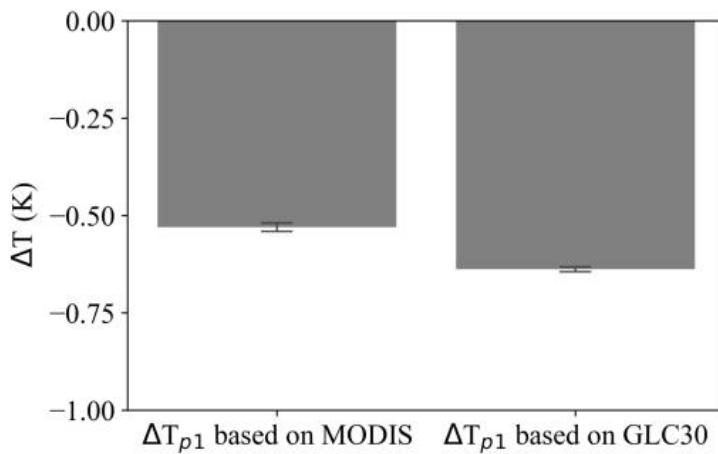
Figure A5. The mixed potential effects (ΔT_{p1}) obtained based on MODIS land-cover data (MCD12Q1) and the land-cover distribution map defined at the threshold of 50% GlobeLand30 at 1 km resolution.
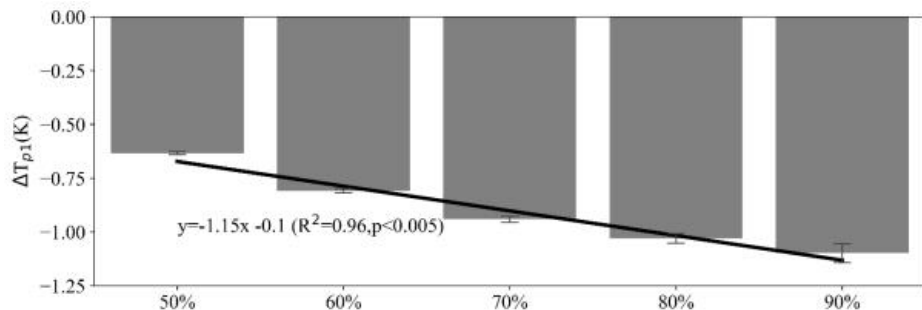

Figure A6. The influence of the forest-cover threshold applied to the land-cover map underlying the estimation of the mixed potential effect (ΔT_{p1}).
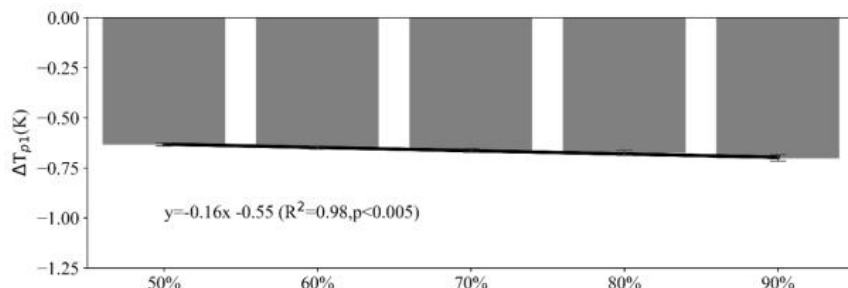

Figure A7. The influence of the openland-cover threshold used to identify a 1km pixel as openland in the estimation of the mixed potential effect (ΔT_{p1}).
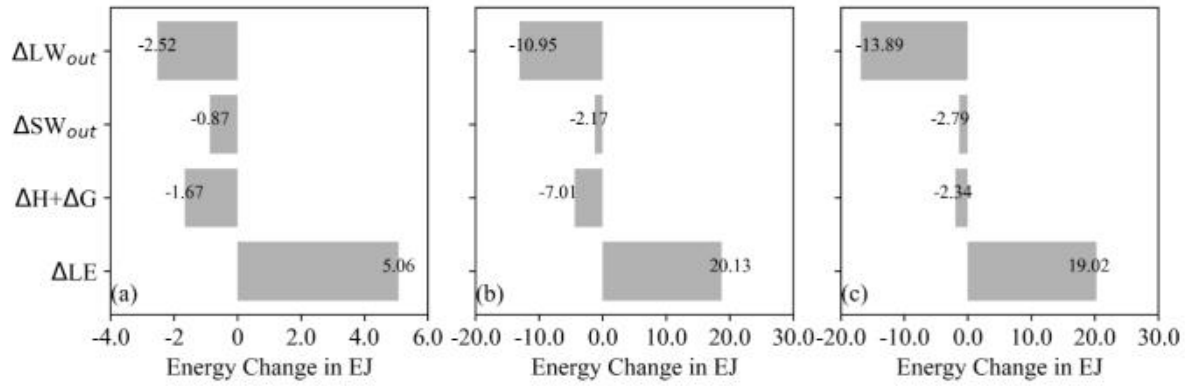
Figure A8. Afforestation-induced cumulative changes in surface energy fluxes (exaJoules) in China for the period 2000–2012 following the approaches of (a) actual effect, (b) mixed potential effect and (c) full potential effect (methods in Appendix Text A1).

Text A1

The cumulative surface energy effect (f_{cum}) in Figure A8 refers to the sum of the flux change (J) from all the samples, while at the same time accounting for the forest change area (m^2). More specifically, the cumulative surface energy change (f_{cum}) can be calculated from equation A1:

$$f_{cum} = \sum_{i=1}^{i=n}(area_i \times F_i) \tag{A1}$$

where F_i is the flux change per unit area (W m^{-2}) for pixel i, n is the total number of samples, and area$_i$ is the forest change area in pixel i.

Data availability

All datasets used in this study are summarized in Table 1 and are openly available. Albedo, transpiration and surface temperature data can be accessed at (https://modis.gsfc.nasa.gov/data/). The Global Forest Change data is available from https://earthenginepartners.appspot.com/science-2013-global-forest/. The land-cover type dataset (GlobeLand30) can be downloaded from http://www.globallandcover.com/. Incoming

714 shortwave radiation data can be accessed at https://ceres.larc.nasa.gov/data/. The elevation data

715 is available from NASA's Shuttle Radar Topography Mission (SRTM) data

716 (https://lpdaac.usgs.gov/products/srtmgl1v003/). Intermediate data and scripts used to generate

717 the results in this study are available from the corresponding author upon reasonable request.

718

719 **Author contributions**

720 Chao Yue and Sebastiaan Luyssaert designed the study. Huanhuan Wang conducted the

721 analysis. All three authors contributed to writing and revision of the text.

722

723 **Competing interests**

724 The authors have the following competing interests: At least one of the (co-)authors is a member

725 of the editorial board of Biogeosciences.

726

731

732 **References**

733 Alkama, R. and Cescatti, A.: Biophysical climate impacts of recent changes in global forest

734   cover, Science, 351, 600–604, https://doi.org/10.1126/science.aac8083, 2016.

735 Bonan, G. B.: Forests and climate change: forcings, feedbacks, and the climate benefits of

736   forests, Science, 320, 1444–1449, https://doi.org/10.1126/science.1155121, 2008.

737 Bryan, B. A., Gao, L., Ye, Y., Sun, X., Connor, J. D., Crossman, N. D., Stafford-Smith, M.,

738   Wu, J., He, C., Yu, D., Liu, Z., Li, A., Huang, Q., Ren, H., Deng, X., Zheng, H., Niu, J.,

Han, G., and Hou, X.: China's response to a national land-system sustainability emergency, Nature, 559, 193–204, https://doi.org/10.1038/s41586-018-0280-2, 2018.

Chen, C., Park, T., Wang, X., Piao, S., Xu, B., Chaturvedi, R. K., Fuchs, R., Brovkin, V., Ciais, P., Fensholt, R., Tømmervik, H., Bala, G., Zhu, Z., Nemani, R. R., and Myneni, R. B.: China and India lead in greening of the world through land-use management, Nat Sustain, 2, 122–129, https://doi.org/10.1038/s41893-019-0220-7, 2019.

Chen, J., Chen, J., Liao, A., Cao, X., Chen, L., Chen, X., He, C., Han, G., Peng, S., and Lu, M.: Global land cover mapping at 30 m resolution: A POK-based operational approach, 103, 7–27, https://doi.org/10.1016/j.isprsjprs.2014.09.002, 2015.

Chen, L. and Dirmeyer, P. A.: Adapting observationally based metrics of biogeophysical feedbacks from land cover/land use change to climate modeling, Environ. Res. Lett., 11, 034002, https://doi.org/10.1088/1748-9326/11/3/034002, 2016.

Chen, H., Zeng, Z., Wu, J., Peng, L., Lakshmi, V., Yang, H., and Liu, J.: Large Uncertainty on Forest Area Change in the Early 21st Century among Widely Used Global Land Cover Datasets, Remote Sensing, 12, 3502, https://doi.org/10.3390/rs12213502, 2020.

Cs, M., G, S., and Y, Z.: Afforestation and forests at the dryland edges: lessons learned and future outlooks. In: Chen J, Wan S, Henebry G, Qi J, Gutman G, Sun G, Kappas M (szerk.) Dryland East Asia: Land dynamics amid social and climate change. HEP Publishers, Beijing & Walter de Gruyter and Co. Berlin, 2013, 245–264, https://doi.org/10.13140/RG.2.1.4325.4487, 2013.

Duveiller, G., Hooker, J., and Cescatti, A.: The mark of vegetation change on Earth's surface energy balance, Nat Commun, 9, 679, https://doi.org/10.1038/s41467-017-02810-8, 2018.

Duveiller, G., Caporaso, L., Abad-Viñas, R., Perugini, L., Grassi, G., Arneth, A., and Cescatti, A.: Local biophysical effects of land use and land cover change: towards an assessment

764   tool   for   policy   makers,   Land   Use   Policy,   91,   104382,

765   https://doi.org/10.1016/j.landusepol.2019.104382, 2020.

766 Fang, J., Guo, Z., Hu, H., Kato, T., Muraoka, H., and Son, Y.: Forest biomass carbon sinks in

767   East Asia, with special reference to the relative contributions of forest expansion and

768   forest   growth,   Global   Change   Biology,   20,   2019–2030,

769   https://doi.org/10.1111/gcb.12512, 2014.

770 Ge, J., Guo, W., Pitman, A. J., De Kauwe, M. G., Chen, X., and Fu, C.: The Nonradiative Effect

771   Dominates Local Surface Temperature Change Caused by Afforestation in China, 32,

772   4445–4471, https://doi.org/10.1175/JCLI-D-18-0772.1, 2019.

773 Hansen, M. C., Potapov, P. V., Moore, R., Hancher, M., Turubanova, S. A., Tyukavina, A.,

774   Thau, D., Stehman, S. V., Goetz, S. J., and Loveland, T. R.: High-resolution global maps

775   of   21st-century   forest   cover   change,   342,   850–853,

776   https://doi.org/10.1126/science.1244693, 2013.

777 Huang, L., Zhai, J., Liu, J., and Sun, C.: The moderating or amplifying biophysical effects of

778   afforestation on CO2-induced cooling depend on the local background climate regimes

779   in   China,   Agricultural   and   Forest   Meteorology,   260–261,   193–203,

780   https://doi.org/10.1016/j.agrformet.2018.05.020, 2018.

781 Jia, G., Shevliakova, E., Artaxo, P., Noblet-Ducoudré, N. D., Houghton, R., Anderegg, W.,

782   Bastos, A., Bernsten, T. K., Cai, P., Calvin, K., Klein, C. D., Humpenöder, F., Kanter,

783   D., McDermid, S., Peñuelas, J., Pradhan, P., Quesada, B., Roe, S., Bernier, P., Espinoza,

784   J. C., Semenov, S., and Xu, X.: Climate Change and Land: an IPCC Special Report on

785   Climate Change, Desertification, Land Degradation, Sustainable Land Management,

786   Food Security, and Greenhouse Gas Fluxes in Terrestrial Ecosystems. 2019.

787 Juang, J.-Y., Katul, G., Siqueira, M., Stoy, P., and Novick, K.: Separating the effects of albedo

788   from eco-physiological changes on surface temperature along a successional

chronosequence in the southeastern United States, Geophys. Res. Lett., 34, 21, https://doi.org/10.1029/2007GL031296, 2007.

Kato, S., Rose, F. G., Rutan, D. A., Thorsen, T. J., Loeb, N. G., Doelling, D. R., Huang, X., Smith, W. L., Su, W., and Ham, S.-H.: Surface Irradiances of Edition 4.0 Clouds and the Earth's Radiant Energy System (CERES) Energy Balanced and Filled (EBAF) Data Product, 31, 4501–4527, https://doi.org/10.1175/JCLI-D-17-0523.1, 2018.

Lee, X., Goulden, M. L., Hollinger, D. Y., Barr, A., Black, T. A., Bohrer, G., Bracho, R., Drake, B., Goldstein, A., Gu, L., Katul, G., Kolb, T., Law, B. E., Margolis, H., Meyers, T., Monson, R., Munger, W., Oren, R., Paw U, K. T., Richardson, A. D., Schmid, H. P., Staebler, R., Wofsy, S., and Zhao, L.: Observed increase in local cooling effect of deforestation at higher latitudes, Nature, 479, 384–387, https://doi.org/10.1038/nature10588, 2011.

Lee, S. and Lee, D. K.: What is the proper way to apply the multiple comparison test?, Korean J Anesthesiol, 71, 353–360, https://doi.org/10.4097/kja.d.18.00242, 2018.

Li, Y., Zhao, M., Motesharrei, S., Mu, Q., Kalnay, E., and Li, S.: Local cooling and warming effects of forests based on satellite observations, Nature Communications, 6, 6603, https://doi.org/10.1038/ncomms7603, 2015.

Li, Y., Zhao, M., Mildrexler, D. J., Motesharrei, S., Mu, Q., Kalnay, E., Zhao, F., Li, S., and Wang, K.: Potential and Actual impacts of deforestation and afforestation on land surface temperature: IMPACTS OF FOREST CHANGE ON TEMPERATURE, J. Geophys. Res. Atmos., 121, 14,372-14,386, https://doi.org/10.1002/2016JD024969, 2016a.

Li, Y., De Noblet-Ducoudré, N., Davin, E. L., Motesharrei, S., Zeng, N., Li, S., and Kalnay, E.: The role of spatial scale and background climate in the latitudinal temperature response to deforestation, Earth Syst. Dynam., 7, 167–181, https://doi.org/10.5194/esd-7-167-

814   2016, 2016b.

815   Li, Y., Piao, S., Chen, A., Ciais, P., and Li, L. Z. X.: Local and teleconnected temperature

816   effects of afforestation and vegetation greening in China, National Science Review, 7,

817   897–912, https://doi.org/10.1093/nsr/nwz132, 2020.

818   Liang, W., Fu, B., Wang, S., Zhang, W., Jin, Z., Feng, X., Yan, J., Liu, Y., and Zhou, S.:

819   Quantification of the ecosystem carrying capacity on China's Loess Plateau, Ecological

820   Indicators, 101, 192–202, https://doi.org/10.1016/j.ecolind.2019.01.020, 2019.

821   Liu, Y.: China's forest resource dynamics based on allometric scaling relationship between

822   forest   area   and   total   stocking   volume,   Afr.   J.   Agric.   Res.,   7,

823   https://doi.org/10.5897/AJAR12.216, 2012.

824   Liu, Z., Ballantyne, A. P., and Cooper, L. A.: Increases in Land Surface Temperature in

825   Response to Fire in Siberian Boreal Forests and Their Attribution to Biophysical

826   Processes, Geophys. Res. Lett., 45, 6485–6494, https://doi.org/10.1029/2018GL078283,

827   2018.

828   Oleson, K., Lawrence, D., Bonan, G., Drewniak, B., Huang, M., Koven, C., Levis, S., Li, F.,

829   Riley, W., Subin, Z., Swenson, S., Thornton, P., Bozbiyik, A., Fisher, R., Heald, C.,

830   Kluzek, E., Lamarque, J.-F., Lawrence, P., Leung, L., and Yang, Z.-L.: Technical

831   description   of   version   4.5   of   the   Community   Land   Model   (CLM),

832   https://doi.org/10.5065/D6RR1W7M, 2013.

833   Pan, Y., Birdsey, R. A., Fang, J., Houghton, R., Kauppi, P. E., Kurz, W. A., Phillips, O. L.,

834   Shvidenko, A., Lewis, S. L., Canadell, J. G., Ciais, P., Jackson, R. B., Pacala, S. W.,

835   McGuire, A. D., Piao, S., Rautiainen, A., Sitch, S., and Hayes, D.: A Large and

836   Persistent   Carbon   Sink   in   the   World's   Forests,   333,   988–993,

837   https://doi.org/10.1126/science.1201609, 2011.

838   Peng, S.-S., Piao, S., Zeng, Z., Ciais, P., Zhou, L., Li, L. Z. X., Myneni, R. B., Yin, Y., and

839 Zeng, H.: Afforestation in China cools local land surface temperature, Proceedings of

840 the National Academy of Sciences, 111, 2915–2919,

841 https://doi.org/10.1073/pnas.1315126111, 2014.Pongratz, J., Schwingshackl, C., Bultan,

842 S., Obermeier, W., Havermann, F., and Guo, S.: Land Use Effects on Climate: Current

843 State, Recent Progress, and Emerging Topics, Curr Clim Change Rep, 7, 99–120,

844 https://doi.org/10.1007/s40641-021-00178-y, 2021.

845 Pitman, A. J., de Noblet-Ducoudré, N., Cruz, F. T., Davin, E. L., Bonan, G. B., Brovkin, V.,

846 Claussen, M., Delire, C., Ganzeveld, L., and Gayler, V.: Uncertainties in climate

847 responses to past land cover change: First results from the LUCID intercomparison

848 study, Geophys. Res. Lett., 36, https://doi.org/10.1029/2009GL039076, 2009.

849 Pitman, A. J., Avila, F. B., Abramowitz, G., Wang, Y. P., Phipps, S. J., and de Noblet-Ducoudré,

850 N.: Importance of background climate in determining impact of land-cover change on

851 regional climate, Nat. Clim. Chang., 1, 472–475, https://doi.org/10.1038/nclimate1294,

852 2011.

853 Qi, Y. and Wu, T.: The politics of climate change in China, WIREs Clim Change, 4, 301–313,

854 https://doi.org/10.1002/wcc.221, 2013.

855 Shen, W., He, J., Huang, C., and Li, M.: Quantifying the Actual Impacts of Forest Cover Change

856 on Surface Temperature in Guangdong, China, Remote Sensing, 12, 2354,

857 https://doi.org/10.3390/rs12152354, 2020.

858 Sulla-Menashe, D. and Friedl, M. A.: User guide to collection 6 MODIS land cover (MCD12Q1

859 and MCD12C1) product, 1–18, 2018.

860 Swann, A. L., Fung, I. Y., and Chiang, J. C.: Mid-latitude afforestation shifts general circulation

861 and tropical precipitation, Proceedings of the National Academy of Sciences, 109, 712–

862 716, https://doi.org/10.1073/pnas.1116706108, 2012.

863 UC Berkely. Spring 2008 - Stat C141/ Bioeng C141 - Statistics for Bioinformatics

864   Winckler, J., Reick, C. H., Bright, R. M., and Pongratz, J.: Importance of Surface Roughness

865   for the Local Biogeophysical Effects of Deforestation, J. Geophys. Res. Atmos., 124,

866   8605–8618, https://doi.org/10.1029/2018JD030127, 2019a.

867   Winckler, J., Lejeune, Q., Reick, C. H., and Pongratz, J.: Nonlocal Effects Dominate the Global

868   Mean Surface Temperature Response to the Biogeophysical Effects of Deforestation,

869   Geophys. Res. Lett., 46, 745–755, https://doi.org/10.1029/2018GL080211, 2019b.

870   Windisch, M. G., Davin, E. L., and Seneviratne, S. I.: Prioritizing forestation based on

871   biogeochemical and local biogeophysical impacts, Nat. Clim. Chang., 11, 867–871,

872   https://doi.org/10.1038/s41558-021-01161-z, 2021.

873   Zeng, Z., Wang, D., Yang, L., Wu, J., Ziegler, A. D., Liu, M., Ciais, P., Searchinger, T. D.,

874   Yang, Z.-L., Chen, D., Chen, A., Li, L. Z. X., Piao, S., Taylor, D., Cai, X., Pan, M.,

875   Peng, L., Lin, P., Gower, D., Feng, Y., Zheng, C., Guan, K., Lian, X., Wang, T., Wang,

876   L., Jeong, S.-J., Wei, Z., Sheffield, J., Caylor, K., and Wood, E. F.: Deforestation-

877   induced warming over tropical mountain regions regulated by elevation, Nature

878   Geoscience, 14, 23–29, https://doi.org/10.1038/s41561-020-00666-0, 2021.

879   Zhang, L., Marron, J. S., Shen, H., and Zhu, Z.: Singular Value Decomposition and Its

880   Visualization, Journal of Computational and Graphical Statistics, 16, 833–854,

881   https://doi.org/10.1198/106186007X256080, 2007.

882   Zhang, Y., Chen, Y., Li, J., and Chen, X.: A Simple Method for Converting 1-km Resolution

883   Daily Clear-Sky LST into Real LST, Remote Sensing, 12, 1641,

884   https://doi.org/10.3390/rs12101641, 2020.

885   Zhao, K. and Jackson, R. B.: Biophysical forcings of land-use changes from potential forestry

886   activities in North America, Ecological Monographs, 84, 329–353,

887   https://doi.org/10.1890/12-1705.1, 2014.

888   Ziter, C. D., Pedersen, E. J., Kucharik, C. J., & Turner, M. G. (2019). Scale-dependent

889   interactions between tree canopy cover and impervious surfaces reduce daytime urban

890   heat during summer. Proceedings of the National Academy of Sciences, 116(15), 7575–

891   7580. https://doi.org/10.1073/pnas.1817561116